

# First- and Second-Order Digital Quantum Simulation of Three-Level Jaynes–Cummings Dynamics on Superconducting Quantum Processors

J. Thirunirai Selvam,<sup>1</sup> S. Saravana Veni,<sup>1,\*</sup> and Ria Rushin Joseph<sup>2,†</sup>

<sup>1</sup>*Department of Physics, Amrita School of Physical Sciences,  
Amrita Vishwa Vidyapeetham, Coimbatore, 641112, Tamil Nadu, India*

<sup>2</sup>*School of IT, Deakin University, Melbourne, Australia*

This work presents a digital quantum simulation of a three-level atomic system interacting with a single-mode electromagnetic field based on the Jaynes–Cummings model, implemented on IBM Quantum superconducting processors. A qutrit is encoded using two physical qubits to represent the atomic states, while an additional qubit encodes the truncated field mode, enabling the realization of effective  $\Lambda$ -type atomic dynamics. The continuous-time light–matter interaction is implemented in a digital form by discretizing the evolution using Suzuki–Trotter decomposition. In contrast to an analog realization, the digital simulation replaces the continuous evolution with a sequence of quantum gates whose parameters are explicitly controlled. Phase evolution arising from the interaction Hamiltonian is digitally encoded using calibrated  $R_Z$  gates, whose rotation angles are fixed by the physically relevant coupling scale and the chosen Trotter time step. State preparation is achieved using Hadamard and parametrized rotation gates, while the interaction dynamics are implemented through controlled operations. A comparative analysis between first- and second-order Trotter implementations reveals a trade-off between digital accuracy and hardware-induced noise. Overall, the results demonstrate that calibrated gate operations and noise-aware circuit design enable reliable digital simulation of multi-level light–matter interactions on noisy intermediate-scale quantum platforms.

## I. INTRODUCTION

Quantum computing exploits the principles of quantum mechanics to perform computational tasks that are intractable for classical computers[1]. Quantum information processing is fundamentally based on quantum bits (qubits), which, unlike classical bits, can exist in coherent superpositions of states and exhibit entanglement. These uniquely quantum features enable powerful computational paradigms that offer exponential or polynomial speedups for problems such as integer factorization, optimization, and the simulation of quantum many-body systems[2, 3].

Among the various physical realizations of qubits, superconducting circuits have emerged as a leading platform due to their scalability, compatibility with established semiconductor fabrication techniques, and fast, high-fidelity gate operations [4, 5]. Superconducting qubits are engineered from nonlinear, non-dissipative electrical circuits incorporating Josephson junctions, which give rise to discrete, quantized energy levels. Operated at cryogenic temperatures, typically below 20 mK, these circuits behave as artificial atoms with controllable parameters [6–10].

The transmon qubit is the most widely used superconducting qubit architecture[11, 12]. It is a modified charge qubit designed to suppress sensitivity to charge noise by increasing the ratio of Josephson energy to charging energy. The resulting weak anharmonicity allows selective control of the lowest two energy levels, which define the computational basis states  $|0\rangle$  and  $|1\rangle$ . Using tunable

couplings and precisely shaped microwave pulses, superconducting qubits can be entangled and manipulated to implement universal quantum logic operations[13, 14]. Large-scale quantum processors developed by companies such as IBM, Google, and Rigetti now incorporate tens to hundreds of superconducting qubits, enabling experimental studies of near-term quantum algorithms and device-level physics[15, 16].

Despite this progress, current quantum processors operate in the Noisy Intermediate-Scale Quantum (NISQ) regime, characterized by limited coherence times and the absence of fully fault-tolerant quantum error correction. Quantum states are highly susceptible to both intrinsic and environmental noise sources, including material defects, control imperfections, and high-energy radiation events. The mitigation of such noise through improved materials, device design, and error-correcting strategies remains a central challenge in superconducting quantum technologies[17, 18].

While the conventional Jaynes–Cummings (JC) model describing the interaction between a two-level atom and a single quantized field mode has been studied extensively, increasing attention has been directed toward multi-level atomic systems owing to their richer internal structure and enhanced control capabilities[19–22]. In particular, three-level atomic configurations such as ladder,  $\Lambda$ -, and V-type systems introduce quantum interference effects that can significantly modify population transfer, coherence properties, and atom–field entanglement dynamics. These features are not only of fundamental interest in quantum optics but are also directly relevant to quantum information processing, quantum control, and state engineering protocols[23–25].

Existing studies on three-level Jaynes–Cummings-type models have largely focused on analytical treatments and

\* s.saravanaveni@cb.amrita.edu

† ria.joseph@deakin.edu.au

idealized numerical simulations, highlighting phenomena such as modified Rabi oscillations, population trapping, and interference-induced suppression or enhancement of entanglement. However, most of these investigations assume noise-free dynamics and do not explicitly address the constraints imposed by contemporary quantum hardware. As a result, the practical feasibility of realizing multi-level light-matter interaction models on present-day quantum processors remains an open and important issue[26, 27]. The rapid development of superconducting quantum processors has opened new avenues for exploring complex quantum dynamical systems beyond the capabilities of classical computation. Among such systems, the Jaynes-Cummings model occupies a central position in quantum optics, cavity quantum electrodynamics, and quantum information science, as it provides a fundamental description of light-matter interaction at the single-quantum level. While the ideal Jaynes-Cummings dynamics are well understood theoretically, extending these models to multi-level atoms and experimentally relevant regimes introduces significant computational and experimental [28–31].

Classical numerical simulations of multi-level atom-field interactions suffer from an exponential growth of the Hilbert space with increasing excitation number and atomic complexity, limiting their applicability to small systems and short evolution times. At the same time, analog quantum simulators based on cavity or circuit QED platforms require precise hardware engineering and offer limited tunability and scalability. Digital quantum simulation using programmable superconducting qubits provides a flexible alternative, enabling systematic control over Hamiltonian parameters, interaction strengths, and evolution times through gate-based implementations[32–34].

In the noisy intermediate-scale quantum (NISQ) era, however, practical quantum simulations are constrained by decoherence, gate imperfections, and readout errors. These limitations impose strict bounds on circuit depth and simulation accuracy, particularly for time-dependent and interacting quantum systems[35, 36]. Therefore, it is essential to develop resource-efficient circuit constructions and benchmarking strategies that balance physical fidelity with experimental feasibility. In this context, the comparison between first- and second-order Suzuki-Trotter decompositions offers valuable insights into the trade-off between digital accuracy and hardware noise[37–39].

Motivated by these challenges, the present work aims to design, implement, and experimentally evaluate optimized quantum circuits for simulating a three-level Jaynes-Cummings system on real superconducting quantum hardware. By integrating physically motivated parameter calibration, hardware-aware fidelity estimation, and systematic backend selection, this study seeks to establish practical guidelines for reliable quantum optical simulations in near-term devices. The results contribute toward bridging the gap between theoretical quantum optics models and their experimental realization on scalable

quantum computing platforms[40–43].

## II. DERIVATION OF ATOM-FIELD DYNAMICS AND ENTANGLEMENT

The interaction between a two-level atom and a single quantized mode of the electromagnetic field provides the simplest fully quantum model for studying light-matter interaction. In cavity and circuit quantum electrodynamics, this interaction is well described by the Jaynes-Cummings Hamiltonian under the rotating-wave approximation (RWA),

$$H = \hbar\omega_f a^\dagger a + \frac{\hbar\omega_a}{2} \sigma_z + \hbar g (a\sigma_+ + a^\dagger\sigma_-), \quad (1)$$

where  $\omega_f$  is the frequency of the cavity field mode and  $\omega_a$  is the atomic transition frequency between the excited state  $|e\rangle$  and the ground state  $|g\rangle$ . The operators  $a^\dagger$  and  $a$  create and annihilate photons in the cavity and satisfy bosonic commutation relations. The Pauli operator  $\sigma_z$  describes the atomic population inversion, while  $\sigma_+$  and  $\sigma_-$  govern atomic excitation and relaxation processes. The coupling constant  $g$  sets the rate at which energy is coherently exchanged between the atom and the field and depends on the dipole moment of the atom and the cavity mode volume.

The rotating-wave approximation is essential in this context because it eliminates rapidly oscillating counter-rotating terms that average out on experimentally relevant time scales. This approximation ensures energy conservation during atom-field interaction and allows for an exact analytical treatment of the dynamics, which is crucial for understanding entanglement generation mechanisms.

Under the resonance condition  $\omega_f = \omega_a$ , the Hamiltonian commutes with the total excitation number operator

$$\hat{N} = a^\dagger a + \sigma_+ \sigma_-, \quad (2)$$

such that

$$[H, \hat{N}] = 0. \quad (3)$$

This conservation law is not merely a mathematical convenience; it reflects the physical fact that excitations are exchanged coherently between the atom and the field without loss. As a result, the full Hilbert space decomposes into invariant subspaces of fixed excitation number. Each subspace is spanned by the states  $\{|e, n\rangle, |g, n+1\rangle\}$ , which share the same total excitation. This restriction dramatically simplifies the dynamics and makes it possible to derive exact time-dependent solutions[44].

Assuming an initial atom-field product state with the atom in its excited state and the field prepared in a Fock state,

$$|\psi(0)\rangle = |e, n\rangle, \quad (4)$$

the system evolution remains confined to the corresponding excitation subspace. Consequently, the time-dependent state can be expressed as

$$|\psi(t)\rangle = c_e(t)|e, n\rangle + c_g(t)|g, n+1\rangle, \quad (5)$$

where the probability amplitudes  $c_e(t)$  and  $c_g(t)$  encode the exchange of excitation between atom and field.

Substituting this state into the time-dependent Schrödinger equation

$$i\hbar \frac{d}{dt} |\psi(t)\rangle = H |\psi(t)\rangle \quad (6)$$

and projecting onto the basis states yields the coupled equations

$$i\dot{c}_e(t) = g\sqrt{n+1}c_g(t), \quad (7)$$

$$i\dot{c}_g(t) = g\sqrt{n+1}c_e(t). \quad (8)$$

The appearance of the factor  $\sqrt{n+1}$  originates from the bosonic nature of the field and highlights the photon-number dependence of the atom-field coupling strength. This dependence is responsible for nonclassical effects such as collapse and revival phenomena when the field is initially in a superposition of Fock states.

Solving the coupled equations with initial conditions  $c_e(0) = 1$  and  $c_g(0) = 0$  gives

$$c_e(t) = \cos(g\sqrt{n+1}t), \quad (9)$$

$$c_g(t) = -i \sin(g\sqrt{n+1}t), \quad (10)$$

leading to the time-evolved state

$$|\psi(t)\rangle = \cos(g\sqrt{n+1}t) |e, n\rangle - i \sin(g\sqrt{n+1}t) |g, n+1\rangle. \quad (11)$$

This solution demonstrates coherent Rabi oscillations between atomic and field excitations with a photon-number-dependent Rabi frequency

$$\Omega_n = 2g\sqrt{n+1}. \quad (12)$$

Such oscillations are a hallmark of strong coupling and have been observed in cavity and circuit QED experiments[45].

To quantify quantum correlations generated during the interaction, the total atom-field density operator is defined as

$$\rho_{AF}(t) = |\psi(t)\rangle\langle\psi(t)|. \quad (13)$$

Although the composite system remains in a pure state, the atomic subsystem alone generally does not. Tracing over the field degrees of freedom,

$$\rho_A(t) = \text{Tr}_F[\rho_{AF}(t)], \quad (14)$$

yields the reduced atomic density matrix

$$\rho_A(t) = \begin{pmatrix} \cos^2(g\sqrt{n+1}t) & 0 \\ 0 & \sin^2(g\sqrt{n+1}t) \end{pmatrix}. \quad (15)$$

The mixed nature of  $\rho_A(t)$  directly reflects the entanglement between the atom and the field, even in the absence of decoherence.

The degree of entanglement is quantified using the atomic von Neumann entropy

$$S_A(t) = -\text{Tr}[\rho_A(t) \ln \rho_A(t)]. \quad (16)$$

Starting from zero for an initially separable state, the entropy increases as atom-field correlations build up and Figure 1 shows the time evolution of the atomic entropy. Starting from a nearly pure atomic state, the entropy initially increases due to atom-field entanglement generated by the interaction. The subsequent oscillatory behavior reflects periodic exchange of quantum information between the atom and the field, analogous to collapse and revival phenomena observed in Jaynes-Cummings dynamics. The saturation of entropy at later times indicates the formation of a quasi-steady entangled state[46].

Beyond two-level systems, multilevel atoms enable richer interference phenomena such as coherent population trapping and electromagnetically induced transparency. We consider a three-level  $\Lambda$ -type atom interacting with a weak probe field and a strong control field.

Under the rotating-wave approximation (RWA), the interaction between the three-level atom and the applied classical fields is described by the time-dependent Hamiltonian

$$H_I(t) = -\frac{\hbar}{2} (g_p(t) \sigma_{31} + g_c(t) \sigma_{32} + \text{H.c.}), \quad (17)$$

where  $\sigma_{31} = |3\rangle\langle 1|$  and  $\sigma_{32} = |3\rangle\langle 2|$  are the atomic transition operators associated with the  $|1\rangle \leftrightarrow |3\rangle$  and  $|2\rangle \leftrightarrow |3\rangle$  transitions, respectively. The quantities  $g_p(t)$  and  $g_c(t)$  denote the time-dependent coupling strengths (Rabi frequencies) of the probe and control fields.

The explicit time dependence of  $g_p(t)$  and  $g_c(t)$  allows for the description of shaped laser pulses or slowly varying field envelopes, enabling dynamical control of the atomic population and coherence. Such temporal modulation plays a crucial role in coherent control protocols, including electromagnetically induced transparency (EIT), adiabatic population transfer, and dark-state formation. The Hermitian conjugate (H.c.) terms ensure that the Hamiltonian remains self-adjoint and account for the reverse atomic transitions.[47].

The Rabi frequencies  $\Omega_p$  and  $\Omega_c$  characterize the strengths of the coherent probe and control fields, respectively, and can be independently tuned experimentally. The resulting dynamics therefore correspond to a coherently driven  $\Lambda$ -type three-level atomic system within the rotating-wave approximation (RWA), rather than an anti-Jaynes-Cummings interaction.

The atomic state is written as

$$|\psi(t)\rangle = c_1(t)|1\rangle + c_2(t)|2\rangle + c_3(t)|3\rangle, \quad (18)$$

where  $|1\rangle$  and  $|2\rangle$  are the two lower states and  $|3\rangle$  is the excited state. Substituting this expansion into the

Schrödinger equation with the RWA interaction Hamiltonian yields the coupled equations of motion

$$\dot{c}_1(t) = i\frac{\Omega_p}{2}c_3(t), \quad (19)$$

$$\dot{c}_2(t) = i\frac{\Omega_c}{2}c_3(t), \quad (20)$$

$$\dot{c}_3(t) = i\frac{\Omega_p}{2}c_1(t) + i\frac{\Omega_c}{2}c_2(t). \quad (21)$$

These equations explicitly show that the excited state  $|3\rangle$  acts as a coherent intermediate level that couples the two lower states through the applied fields. Quantum interference between the probe-driven and control-driven excitation pathways leads to coherent population oscillations and, for suitable parameter regimes, partial population trapping. This mechanism underlies phenomena such as dark-state formation and electromagnetically induced transparency (EIT), which have no analogue in two-level atomic systems [48].

The level populations are obtained from the reduced atomic density matrix as

$$P_j(t) = \langle j|\rho_A(t)|j\rangle, \quad j = 1, 2, 3. \quad (22)$$

Figure 1 illustrates the temporal evolution of these populations. The oscillatory transfer of population between the three levels reflects coherent multi-frequency beating driven by the probe and control fields. The apparent envelope modulation arises from interference between distinct excitation pathways, rather than from dissipative decay processes (unless explicit decoherence terms are included).

Such behavior is a hallmark of coherently driven three-level  $\Lambda$  systems and demonstrates the richer coherence control and population dynamics achievable beyond the standard two-level Jaynes–Cummings model.

### III. CONSTRUCTION OF FIRST- AND SECOND-ORDER DIGITAL CIRCUITS FOR A THREE-LEVEL JAYNES–CUMMINGS SYSTEM

In this work, the dynamics of a three-level atom interacting with a quantized field are digitally simulated using superconducting qubits on the IBM Quantum platform. The circuit constructions shown in Fig. 2, 3 are obtained by systematically mapping the continuous Jaynes–Cummings Hamiltonian onto elementary quantum gates through Suzuki–Trotter decomposition[49].

#### III.0.1. Encoding of Atomic and Field Basis States

The physical system consists of a truncated single-mode field and a three-level atom with states

$$|g\rangle, \quad |e\rangle, \quad |f\rangle. \quad (23)$$

To represent this system on qubits, we employ a binary encoding scheme. The field mode is truncated to the

vacuum and one-photon subspace and encoded as

$$|0\rangle_f \leftrightarrow |0\rangle_{q_0}, \quad |1\rangle_f \leftrightarrow |1\rangle_{q_0}. \quad (24)$$

The atomic levels are encoded using two qubits as

$$|g\rangle \equiv |00\rangle_{q_1 q_2}, \quad (25)$$

$$|e\rangle \equiv |10\rangle_{q_1 q_2}, \quad (26)$$

$$|f\rangle \equiv |11\rangle_{q_1 q_2}. \quad (27)$$

The three-level atom is encoded using two qubits  $(q_1, q_2)$ , where the states  $|g\rangle$ ,  $|e\rangle$ , and  $|f\rangle$  are mapped to  $|00\rangle$ ,  $|10\rangle$ , and  $|11\rangle$ , respectively. The computational state  $|01\rangle$  is excluded, imposing the selection rule  $q_2 = 1 \Rightarrow q_1 = 1$ . This constraint ensures that the higher atomic level can only be populated after occupation of the intermediate level, consistent with the ladder structure of a physical three-level atom. As a result, the dynamics remain confined to physically allowed atomic configurations.

The complete atom–field basis is therefore written as

$$|n\rangle_f \otimes |j\rangle_a \equiv |q_0 q_1 q_2\rangle, \quad n = 0, 1, \quad j \in \{g, e, f\}. \quad (28)$$

Measurement outcomes are displayed using Qiskit’s conventional classical-bit ordering  $|q_2 q_1 q_0\rangle$  (left-to-right), where the rightmost bit corresponds to qubit  $q_0$ . Accordingly, all physical interpretations of bitstrings in figures use  $q_0$  as the field qubit and  $(q_1, q_2)$  as the atomic register.

#### III.0.2. Hamiltonian Representation in the Encoded Basis

After truncation, the Jaynes–Cummings Hamiltonian is written as

$$H = H_f + H_a + H_{\text{int}}, \quad (29)$$

with

$$H_f = \omega_f |1\rangle_f \langle 1|, \quad (30)$$

$$H_a = \sum_{j=g,e,f} \omega_j |j\rangle \langle j|, \quad (31)$$

$$H_{\text{int}} = \sum_{j=g,e} g_j (a^\dagger |j\rangle \langle j+1| + a |j+1\rangle \langle j|). \quad (32)$$

In the single-excitation manifold,

$$\mathcal{H}_1 = \text{span}\{|g, 1\rangle, |e, 0\rangle\}, \quad (33)$$

the interaction Hamiltonian reduces to

$$H_{\text{int}}^{(1)} = g_1 \sigma_x. \quad (34)$$

Thus, the fundamental atom–field coupling corresponds to a rotation around the  $x$ -axis in this subspace.

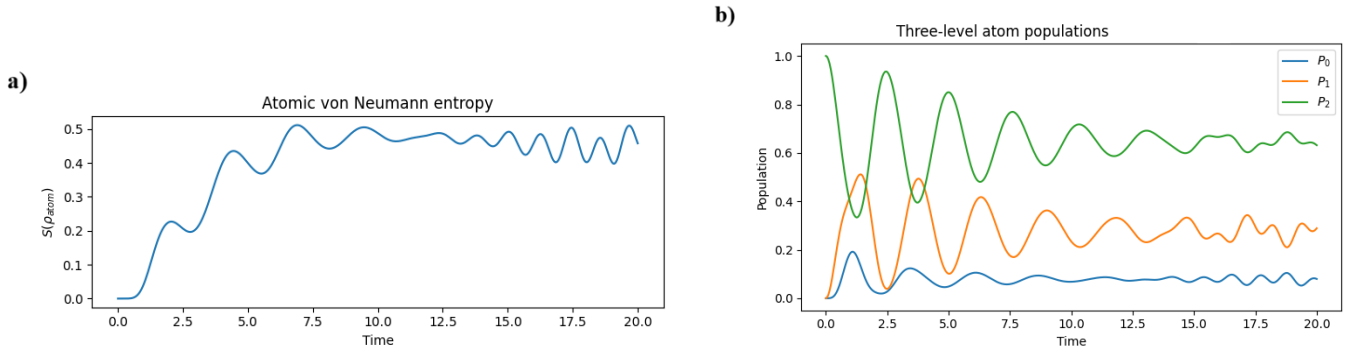


FIG. 1. **(a)** The initial coherent field state, where the atom is prepared in the excited state and the cavity field is in a coherent state with mean photon number  $\bar{n}$ . Since a coherent state is a superposition of many Fock states, each photon-number component evolves with a slightly different Rabi frequency. This results in dephasing among the components, causing the atomic von Neumann entropy to increase and exhibit oscillatory behavior. The entropy does not return exactly to zero within the plotted time range because the revival time is longer than the displayed interval. No decoherence or dissipation is included in the numerical simulation; the observed behavior arises purely from coherent, unitary Jaynes–Cummings dynamics. **(b)** Time evolution of the populations of the three atomic levels under anti-Jaynes–Cummings couplings. The populations  $P_0$ ,  $P_1$ , and  $P_2$  exhibit coherent oscillations and population redistribution, indicating reversible excitation exchange and  $\Lambda$ -type three-level atomic dynamics.

### III.0.3. First-Order Suzuki–Trotter Circuit Construction

In the first-order approximation, the time-evolution operator is decomposed as

$$U(\Delta t) \approx e^{-iH_f \Delta t} e^{-iH_a \Delta t} e^{-iH_{\text{int}} \Delta t}. \quad (35)$$

Each factor is implemented as an independent circuit block.

**III.0.3.1. Field Evolution Block** After truncation of the cavity field Hilbert space to  $\{|0\rangle_f, |1\rangle_f\}$ , the free-field Hamiltonian reads

$$H_f = \omega_f |1\rangle_f \langle 1| = \frac{\omega_f}{2} (I - Z_f), \quad (36)$$

where  $Z_f$  is the Pauli- $Z$  operator acting on the field qubit.

The corresponding time-evolution operator for a single Suzuki–Trotter step  $\Delta t$  is diagonal and given by

$$U_f(\Delta t) = e^{-iH_f \Delta t} = \text{diag}(1, e^{-i\omega_f \Delta t}) \quad (37)$$

$$= e^{-i\omega_f \Delta t / 2} R_Z(-\omega_f \Delta t). \quad (38)$$

The global phase factor  $e^{-i\omega_f \Delta t / 2}$  is physically irrelevant and may be discarded. Therefore, the free-field evolution is implemented digitally by a single  $R_Z(-\omega_f \Delta t)$  gate acting on the field qubit.

If a weakly excited field state is required (for example, to represent a truncated coherent state), this is not generated by the free-field propagator itself. Instead, it is prepared during the initial state preparation using a small  $R_Y$  rotation,

$$R_Y(\theta_f) = e^{-i\theta_f \sigma_y / 2}, \quad \theta_f \ll 1, \quad (39)$$

which creates a controlled superposition between the vacuum and one-photon states. The subsequent free-field evolution then correctly accumulates relative phases through the  $R_Z$  rotation.

**III.0.3.2. Atomic Energy Block** The atomic Hamiltonian is diagonal in the computational basis and leads to relative phase accumulation. This is implemented using  $R_Z$  rotations,

$$R_Z(\theta_j) = e^{-i\theta_j \sigma_z / 2}, \quad \theta_j = \omega_j \Delta t, \quad (40)$$

applied to the atomic qubits.

These gates reproduce the dynamical phases of the energy levels.

**III.0.3.3. Interaction Block** The interaction term produces coherent exchange

$$|g, 1\rangle \leftrightarrow |e, 0\rangle. \quad (41)$$

Its evolution operator is

$$e^{-ig_1 \Delta t \sigma_x} = R_X(2g_1 \Delta t). \quad (42)$$

Since controlled  $R_X$  gates are not native, we use the identity

$$R_X(\phi) = H R_Z(\phi) H. \quad (43)$$

Therefore, the interaction is implemented as

$$C(H) C(R_Z) C(H), \quad (44)$$

resulting in the characteristic

$$\text{CX-H-RZ-H-CX}$$

structure.

**III.0.3.4. Role of the  $\text{rccx}$  Gate** The  $\text{rccx}$  gate realizes a relative-phase Toffoli operation,

$$|a, b, c\rangle \rightarrow |a, b, c \oplus (ab)\rangle. \quad (45)$$

It ensures that excitation exchange occurs only when the atomic register is in allowed states. This gate enforces the exclusion of  $|01\rangle$  and prevents unphysical transitions.

Thus, in the first-order circuit,  $\text{rccx}$  acts as a digital selection-rule operator.

### III.0.4. Second-Order Suzuki–Trotter Circuit Construction

To improve accuracy, the second-order decomposition is used,

$$U(\Delta t) \approx e^{-i(H_f+H_a)\Delta t/2} e^{-iH_{\text{int}}\Delta t} e^{-i(H_f+H_a)\Delta t/2}. \quad (46)$$

This symmetric structure cancels first-order Trotter errors.

*III.0.4.1. Half-Step Free Evolution* The free evolution operators are split into half-steps,

$$R_Y(\theta_f/2), \quad R_Z(\theta_j/2). \quad (47)$$

These gates appear at the beginning and end of the circuit, producing time-reversal symmetry.

*III.0.4.2. Enhanced Interaction Structure* The second-order circuit includes multiple `rccx` gates and additional atomic registers. This is required to implement higher-order transitions such as

$$|e, 1\rangle \leftrightarrow |f, 0\rangle. \quad (48)$$

These processes depend simultaneously on several qubits and therefore require multi-controlled operations.

Ancillary qubits are introduced to decompose these operations into hardware-compatible gates.

*III.0.4.3. Suppression of Digital Errors* Due to the symmetric Suzuki–Trotter decomposition, the leading-order digital approximation errors scale differently for first- and second-order formulas. For a single Trotter step  $\Delta t$ , the corresponding propagators satisfy

$$U_{1\text{st}}(\Delta t) = e^{-iH\Delta t} + \mathcal{O}(\Delta t^2), \quad (49)$$

$$U_{2\text{nd}}(\Delta t) = e^{-iH\Delta t} + \mathcal{O}(\Delta t^3). \quad (50)$$

As a result, the second-order Suzuki–Trotter scheme significantly suppresses intrinsic digitization errors at fixed time step  $\Delta t$ , leading to reduced phase drift, improved excitation-number conservation, and suppression of unphysical population leakage. This improvement comes at the cost of a deeper circuit and therefore increased exposure to hardware noise, reflecting the fundamental trade-off between digital accuracy and experimental robustness.

### III.0.5. Physical Interpretation of the Gate Structure

Each group of gates in the circuit has a direct physical meaning:

- $R_Y$  gates simulate field excitation and depletion.
- $R_Z$  gates encode atomic and field energy shifts.
- $H-R_Z-H$  blocks implement exchange interactions.
- `rccx` gates enforce atomic selection rules.
- Ancillary qubits enable higher-order conditioning.

Together, these operations reproduce Rabi oscillations, population transfer, and atom–field entanglement.

### III.0.6. Continuous-Time Limit and Fixing of $R_Z$ Gate Parameters

After  $N$  Suzuki–Trotter steps, the digitally implemented time evolution is

$$U(t) \approx [U_{2\text{nd}}(\Delta t)]^N, \quad t = N\Delta t. \quad (51)$$

In the formal limit  $\Delta t \rightarrow 0$ , the Trotterized evolution converges to

$$U(t) \rightarrow e^{-iHt}, \quad (52)$$

thereby recovering the continuous-time Jaynes–Cummings dynamics. The constructed circuits thus provide a controlled and systematic digital approximation to the underlying atom–field interaction.

In a gate-based realization, the continuous evolution must be discretized and mapped onto elementary quantum gates. After truncation of the cavity Hilbert space and qubit encoding, the Jaynes–Cummings Hamiltonian can be expressed as a finite sum of Pauli operators,

$$H = \sum_k h_k P_k, \quad (53)$$

where  $P_k$  are Pauli strings and  $h_k$  are the corresponding coefficients with dimensions of angular frequency. Within a Suzuki–Trotter step of duration  $\Delta t$ , each diagonal Pauli contribution generates a phase evolution of the form

$$e^{-ih_k Z \Delta t} = R_Z(\theta_k), \quad (54)$$

where, following the Qiskit convention  $R_Z(\theta) = e^{-i\theta Z/2}$ , the rotation angle is

$$\theta_k = 2h_k \Delta t. \quad (55)$$

The physically relevant scale of the coefficients  $h_k$  is fixed by the atom–field coupling strength of the Jaynes–Cummings model. In the cavity-QED experiment of Brune *et al.*, the coupling strength is  $g \equiv V_0 = 2\pi \times 25$  kHz, which sets the fastest coherent timescale of the dynamics[50]. That experiment realizes the evolution as a continuous-time analog process and does not introduce a discrete time step. In contrast, in a digital simulation the time step  $\Delta t$  is a numerical control parameter that must be chosen to balance Suzuki–Trotter error against hardware noise, as discussed in Ref [51].

Following standard practice in digital quantum simulation, we choose  $\Delta t$  such that the phase accumulated during one step due to the dominant coupling scale remains small,

$$g\Delta t \lesssim 0.1\text{--}0.2 \text{ rad}, \quad (56)$$

which suppresses leading Trotter errors while keeping the circuit depth experimentally feasible. For the coupling strength reported in Ref. , this condition yields a timestep  $\Delta t$  of order  $1 \mu\text{s}$ . Substituting this value into  $\theta_k = 2h_k \Delta t$ , with  $h_k$  of order  $g$ , naturally results in  $R_Z$  rotation angles in the range  $\theta_k \sim 0.1\text{--}0.2$  rad.

Therefore, the  $R_Z$  gate parameters used in the circuit are not arbitrary but are fixed by matching the experimentally relevant Jaynes–Cummings coupling scale to the digital Suzuki–Trotter discretization strategy. This procedure provides a physically motivated and systematically controllable link between the analog cavity-QED experiment and its gate-based digital quantum simulation.

#### IV. EXPONENTIAL ERROR MODEL AND CIRCUIT FIDELITY

The exponential fidelity model employed in this work is based on the accumulation of small, approximately independent error probabilities associated with quantum gate operations and measurements in noisy intermediate-scale quantum (NISQ) hardware. In superconducting processors, each quantum gate is implemented as a noisy quantum channel affected by decoherence, control imperfections, and readout noise. When such channels are applied sequentially, the probability that the ideal quantum state is preserved decreases exponentially with the total error strength.

Under the assumption of Markovian and uncorrelated noise, the overall circuit fidelity can be approximated as the product of the individual gate and measurement success probabilities. For a sequence of operations with small error probabilities  $p_i \ll 1$ , the fidelity can be written as  $F = \prod_i (1 - p_i)$ , which reduces to the exponential form  $F = \exp[-(E_S + E_T + E_M)]$  using the approximation  $\ln(1 - x) \approx -x$ . Here,  $E_S$ ,  $E_T$ , and  $E_M$  denote the cumulative error contributions from single-qubit gates, two-qubit gates, and measurements, respectively, obtained from experimental calibration data.

Using the exponential error accumulation model, the effective circuit fidelity is given by

$$F = \exp[-(E_S + E_T + E_M)]. \quad (57)$$

From the hardware calibration data of the *ibm.torino* backend, the cumulative error contributions are obtained as follows.

For single-qubit operations, the circuit contains five  $SX$ -equivalent gates with a median error rate of  $3.086 \times 10^{-4}$ . The cumulative single-qubit error is

$$E_S = 5 \times 3.086 \times 10^{-4} = 1.543 \times 10^{-3}. \quad (58)$$

For two-qubit entangling operations, the circuit contains two relative-phase Toffoli (RCCX) blocks. Each RCCX gate is conservatively decomposed into three  $CZ$  gates, and the median  $CZ$  gate error is  $2.437 \times 10^{-3}$ . Therefore,

$$E_T = 6 \times 2.437 \times 10^{-3} = 1.462 \times 10^{-2}. \quad (59)$$

For readout operations, three qubits are measured, each with a median measurement error of  $2.95 \times 10^{-2}$ . The cumulative measurement error is

$$E_M = 3 \times 2.95 \times 10^{-2} = 8.85 \times 10^{-2}. \quad (60)$$

Substituting these contributions into the fidelity expression yields

$$F = \exp[-(0.001543 + 0.01462 + 0.0885)] \quad (61)$$

$$= \exp(-0.10466). \quad (62)$$

Evaluating the exponential gives

$$F \approx 0.9007 \approx 90.1\%. \quad (63)$$

This numerical estimate indicates that the implemented circuit preserves the ideal quantum state with approximately 90% probability under current hardware conditions. The dominant contribution arises from measurement errors, highlighting the importance of readout-error mitigation techniques for improving experimental performance.

Substituting the calibrated error parameters of the *ibm.torino* backend into this model yields an estimated circuit fidelity of approximately 90%, indicating that the implemented circuit preserves the ideal quantum state with high probability under current hardware conditions. Unlike ideal-state fidelity used in noiseless simulations, which compares exact and simulated quantum states, this processor-level fidelity incorporates realistic hardware imperfections and provides a scalable performance metric without requiring full quantum state tomography.

Although the estimated fidelity demonstrates the suitability of the circuit for near-term quantum simulations on superconducting platforms, the dominant limitation arises from readout errors, which remain significantly larger than gate errors. To improve the reliability of future experiments, calibration-based estimates may be complemented with empirical verification techniques, such as randomized benchmarking for gate characterization, measurement-error mitigation using calibration matrices, and state fidelity estimation via quantum state tomography for small-scale circuits[52, 53].

The same circuit was run and analyzed on several IBM superconducting quantum processors, such as *ibm.fez* and *ibm.marrakesh*, in addition to the *ibm.torino* backend mentioned above. This was done to make a systematic comparison of fidelity between different hardware generations and calibration regimes. For each processor, the method for estimating fidelity was the same. The error contributions came from the backend calibration data for single-qubit gates, two-qubit entangling gates, and measurement operations.

##### IV.1. First-Order Output Characteristics of the Three-Level Jaynes–Cummings Simulation

Figure 4 presents the measurement outcomes obtained from the first-order digital (Trotterized) simulation of a three-level Jaynes–Cummings system executed on different IBM quantum processors. At first order, the dynamics are expected to remain predominantly confined to the excitation-conserving subspace, with higher-order transitions ideally suppressed. The output distributions

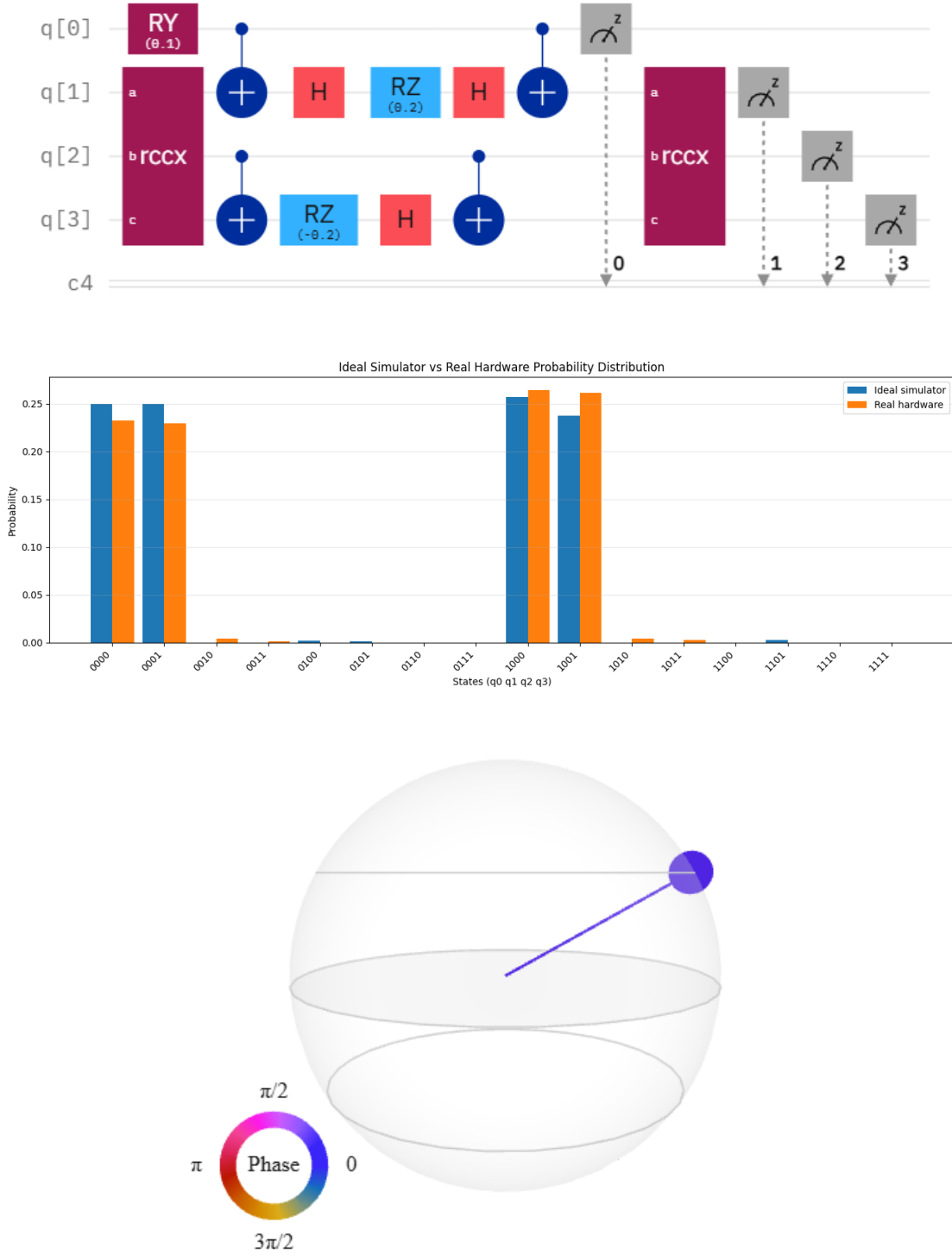


FIG. 2. First-order Suzuki–Trotter simulation of the three-level Jaynes–Cummings model. **(a)** Digital quantum circuit implementing the first-order decomposition of the interaction Hamiltonian. **(b)** Measurement probability distribution obtained from 1024 shots on real hardware, showing dominant populations within allowed excitation subspaces. In comparison with the corresponding ideal (noise-free) simulator, small but nonzero populations appear in classically forbidden states, arising from gate imperfections and decoherence. **(c)** Q-sphere plots are generated from simulator-derived statevectors (or reconstructed quantum states), whereas hardware executions directly yield measurement counts in selected bases. Consequently, Q-sphere visualizations should be interpreted as simulation-based diagnostics of phase and amplitude structure, unless full or partial quantum state tomography or an entanglement witness is additionally performed.

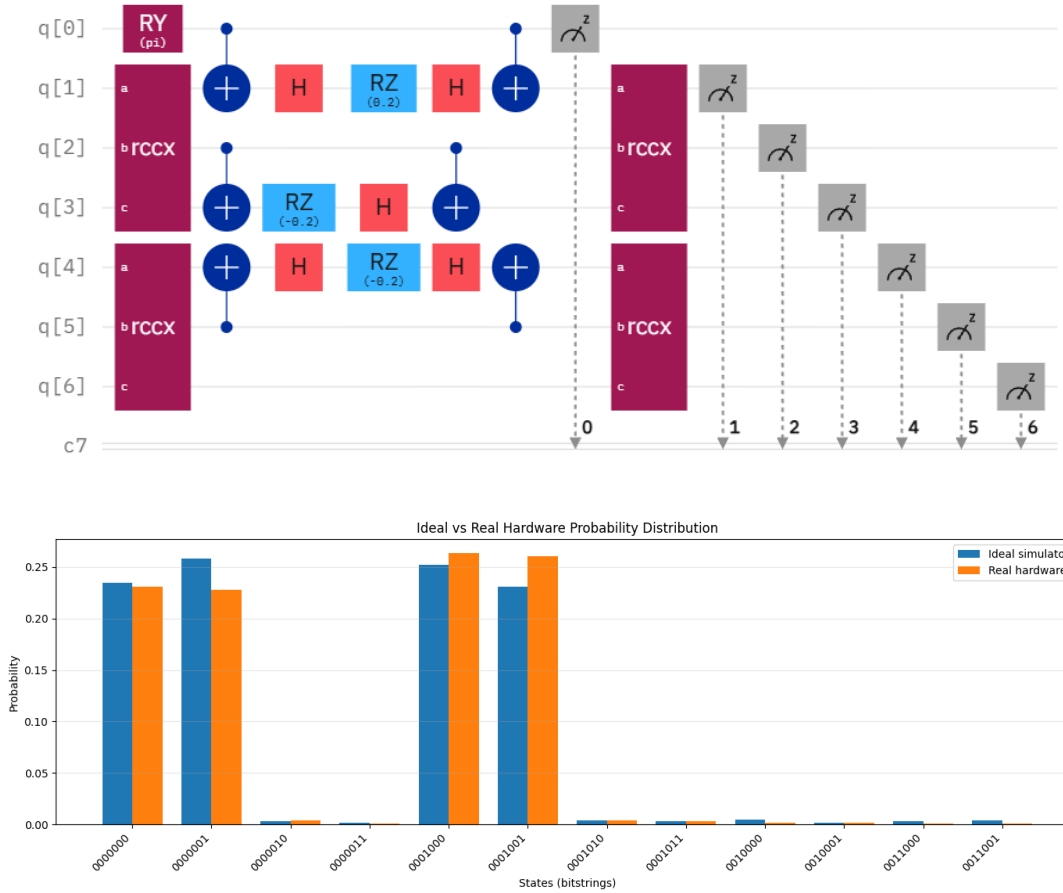


FIG. 3. Second-order Suzuki–Trotter simulation of the three-level Jaynes–Cummings model. **(a)** Symmetric second-order digital circuit with half-step free evolutions and a full interaction block. **(b)** Measurement probability distribution obtained from 1024 shots on real hardware. In comparison with the corresponding ideal (noise-free) simulator, the experimental distribution preserves the dominant population structure and suppresses dynamically forbidden states, while showing residual population leakage due to gate imperfections, decoherence, and readout errors inherent to NISQ devices.

therefore provide a direct experimental signature of how faithfully the leading-order Jaynes–Cummings physics is preserved on each backend.

For the *ibm\_torino* processor, the probability distribution is sharply concentrated in a small number of basis states associated with first-order, excitation-preserving evolution. The strong suppression of nominally forbidden states indicates that higher-order digital errors and noise-induced transitions remain subdominant. This behavior signifies that the measured dynamics are governed primarily by the intended first-order Jaynes–Cummings interaction, with minimal contamination from effective higher-order processes.

In contrast, the output obtained from the *ibm\_marrakesh* backend shows a broader distribution. While the dominant first-order-allowed states remain clearly visible, noticeable population appears in states that should be weakly occupied at first order. This population leakage reflects partial degradation of the leading-order dynamics, where accumulated digital error and decoherence introduce effective corrections beyond the ideal first-order evolution

The *ibm\_fez* processor exhibits the strongest deviation from ideal first-order behavior. Here, the measurement probabilities are distributed across a larger number of basis states, and the contrast between excitation-conserving and suppressed states is significantly reduced. Such broadening indicates that noise and error terms effectively compete with, and partially overwhelm, the intended first-order Jaynes–Cummings dynamics, resulting in pronounced higher-order artifacts in the observed outputs.

Overall, the progressive spreading of measurement probability from *ibm\_torino* to *ibm\_marrakesh* and finally to *ibm\_fez* provides a clear hierarchy of first-order digital fidelity. Sharper confinement of population within the excitation-conserving subspace directly correlates with stronger preservation of first-order Jaynes–Cummings physics, while broader distributions signal increased influence of effective higher-order and noise-induced processes. the highest overall circuit fidelity.

## IV.2. Second-Order Output Characteristics of the Three-Level Jaynes–Cummings Simulation

Figure 5 shows the measurement outcomes obtained from the second-order digital (Trotterized) simulation of a three-level Jaynes–Cummings system. At second order, leading-order digital errors are partially cancelled, resulting in improved approximation of the ideal Jaynes–Cummings evolution. This improvement is directly reflected in the structure of the measured output distributions.

For the *ibm\_torino* processor, the second-order results display a visibly sharper concentration of probability within the excitation-conserving subspace when compared to the first-order case. Previously leaked populations are significantly suppressed, and the dominant Jaynes–Cummings-allowed states exhibit enhanced contrast. This behavior indicates that second-order error cancellation effectively reduces spurious transitions, allowing the intended coherent dynamics to dominate.

The *ibm\_marrakesh* backend also benefits from second-order digital evolution. While some asymmetry and background population remain, the distribution shows noticeable reduction in leakage relative to the first-order results. The persistence of dominant excitation-preserving states suggests improved retention of Jaynes–Cummings dynamics, though residual decoherence limits full recovery of ideal behavior.

In the case of the *ibm\_fez* processor, second-order Trotterization leads to partial improvement in the output distribution, with modest suppression of unintended states. However, the probability remains spread across a larger number of basis states compared to the other backends, indicating that hardware noise competes with the benefits of higher-order digital error cancellation.

Overall, the second-order measurement outcomes demonstrate a clear enhancement in state selectivity and excitation-number conservation relative to first-order implementations. Sharper probability confinement and reduced leakage confirm that second-order digital simulation provides a more faithful representation of three-level Jaynes–Cummings dynamics, particularly on higher-fidelity hardware.

### IV.2.1. Comparison of First- and Second-Order Suzuki–Trotter Fidelity

Figure 6 compares the estimated circuit fidelities obtained for first-order and second-order Suzuki–Trotter decompositions executed on different IBM Quantum processors. The fidelity values are evaluated using a hardware-calibrated first-order error accumulation model that incorporates single-qubit gate errors, two-qubit entangling gate errors, and measurement errors.

For the first-order Suzuki–Trotter circuit, the highest fidelity is achieved on the *ibm\_marrakesh* backend, with an estimated fidelity of approximately 94.6%, closely followed by *ibm\_fez* at 94.5%. In contrast, *ibm\_torino* ex-

hibits a lower fidelity of about 90.0%, primarily predicted by its larger median readout error and earlier-generation Heron r1 architecture. These results indicate that Heron r2 processors provide superior performance for shallower, first-order Trotter circuits.

For the second-order Suzuki–Trotter circuit, which involves a greater number of multi-qubit gates and measurement operations, the overall fidelity is reduced across all processors. Nevertheless, *ibm\_marrakesh* again yields the highest fidelity of approximately 88.4%, marginally outperforming *ibm\_fez* at 88.1%, while *ibm\_torino* shows a more pronounced degradation to about 78.7%. This larger fidelity loss on *ibm\_torino* highlights the increased sensitivity of higher-order Trotter circuits to two-qubit and readout errors.

Overall, the results demonstrate that *ibm\_marrakesh* provides the best performance for both first-order and second-order Suzuki–Trotter implementations, while second-order decompositions, although theoretically more accurate, incur additional hardware-induced errors that limit suggest a trade-off between algorithmic accuracy and experimental fidelity on current noisy intermediate-scale quantum devices.

We compared the performance of first- and second-order digital implementations of the three-level Jaynes–Cummings dynamics across different IBM Quantum backends.

At the first-order level, the *ibm\_torino* processor exhibits the best performance, with measurement outcomes strongly confined to the excitation-conserving subspace and minimal population leakage. The *ibm\_marrakesh* backend shows moderate deviations, including asymmetry in population distribution and increased leakage into non-ideal states, while *ibm\_fez* presents the largest spread across computational basis states, indicating stronger sensitivity to hardware noise and digital errors.

For the second-order digital implementation, all backends demonstrate improved behavior due to partial cancellation of leading-order Trotter errors. Among them, *ibm\_torino* again provides the most accurate results, showing sharper state selectivity and enhanced suppression of spurious transitions. The *ibm\_marrakesh* processor benefits noticeably from the higher-order scheme, with reduced leakage compared to the first-order case, whereas the improvement on *ibm\_fez* remains limited by intrinsic noise and gate errors.

Overall, the second-order digital simulation consistently outperforms the first-order implementation in preserving excitation-number conservation and reducing unphysical population spreading. Across all examined backends, *ibm\_torino* emerges as the most reliable platform for realizing higher-fidelity three-level Jaynes–Cummings dynamics. These results highlight the importance of combining higher-order digital schemes with high-fidelity quantum hardware for accurate multi-level quantum simulations on noisy intermediate-scale quantum devices.

This apparent discrepancy originates from the fundamentally different nature of the two performance metrics. The fidelity values represent an aggregate, calibration-

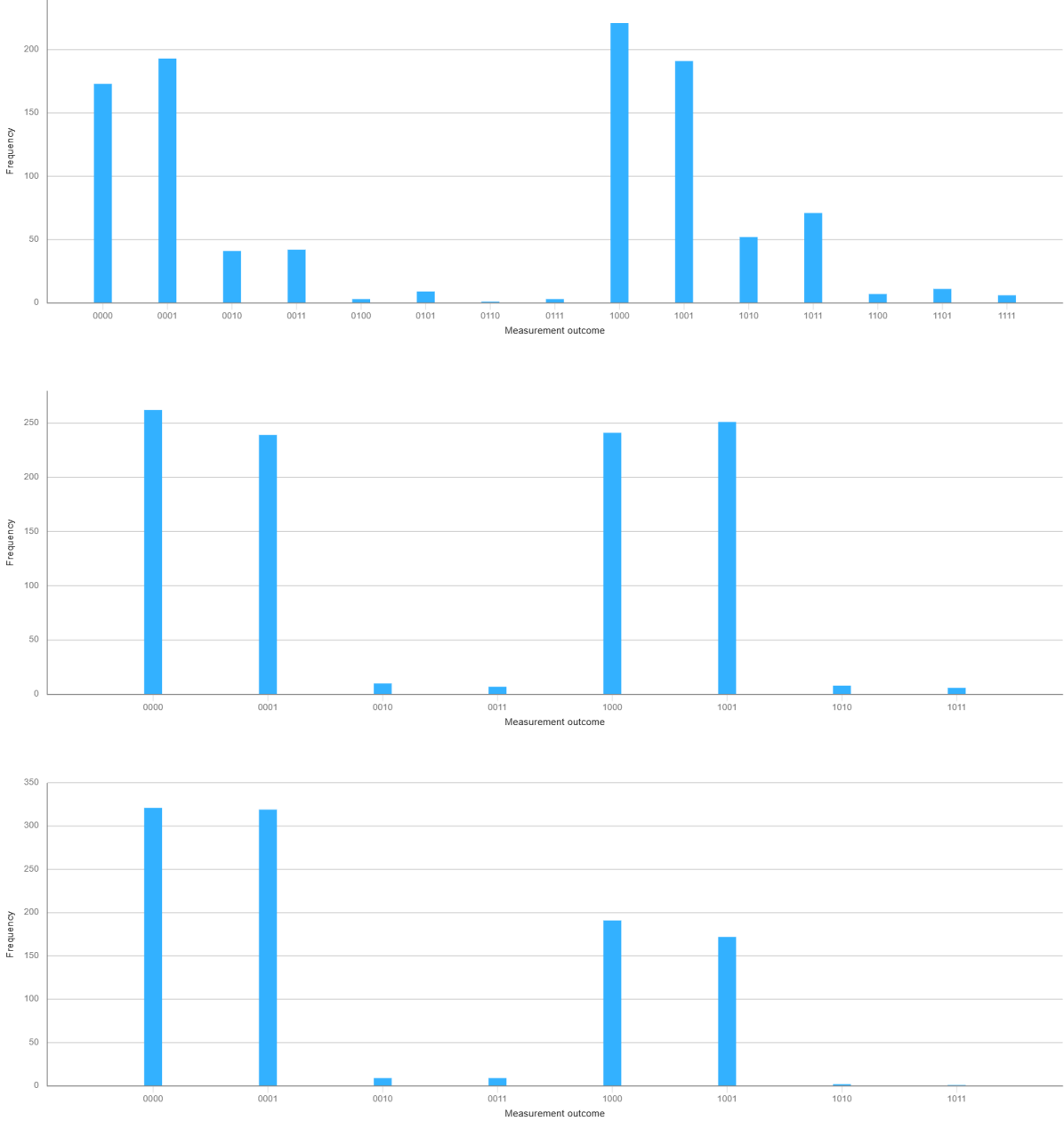


FIG. 4. Measurement outcomes from the first-order digital simulation of the three-level Jaynes–Cummings system executed on the *ibm\_torino*, *ibm\_marrakesh*, and *ibm\_fez* processors. The probability distributions exhibit population leakage and asymmetry across backends, reflecting the sensitivity of first-order Trotterization to digital errors and hardware noise. Bitstrings are ordered as  $|q_2 q_1 q_0\rangle$ , where  $q_2$  encodes the truncated cavity photon number.

based estimate that provides a global measure of hardware quality, averaged over all operations in the circuit. While such a metric is useful for benchmarking general-purpose circuit execution, it does not directly quantify how well specific dynamical constraints or symmetry-preserving features of a quantum model are maintained.

The calibration-based fidelity values provide a coarse-grained assessment of hardware quality, averaged over all gate and measurement operations in the circuit. From this perspective, the *ibm\_marrakesh* processor achieves

the highest overall fidelity for both first-order ( $\sim 94.6\%$ ) and second-order ( $\sim 88.4\%$ ) Suzuki–Trotter implementations, closely followed by *ibm\_fez*, while *ibm\_torino* exhibits lower aggregate fidelity, particularly for the deeper second-order circuit. These results reflect the cumulative impact of two-qubit gate and readout errors, which become increasingly significant for higher-order Trotter decompositions.

In contrast, the frequency (measurement) distributions provide a more sensitive and physically meaningful probe

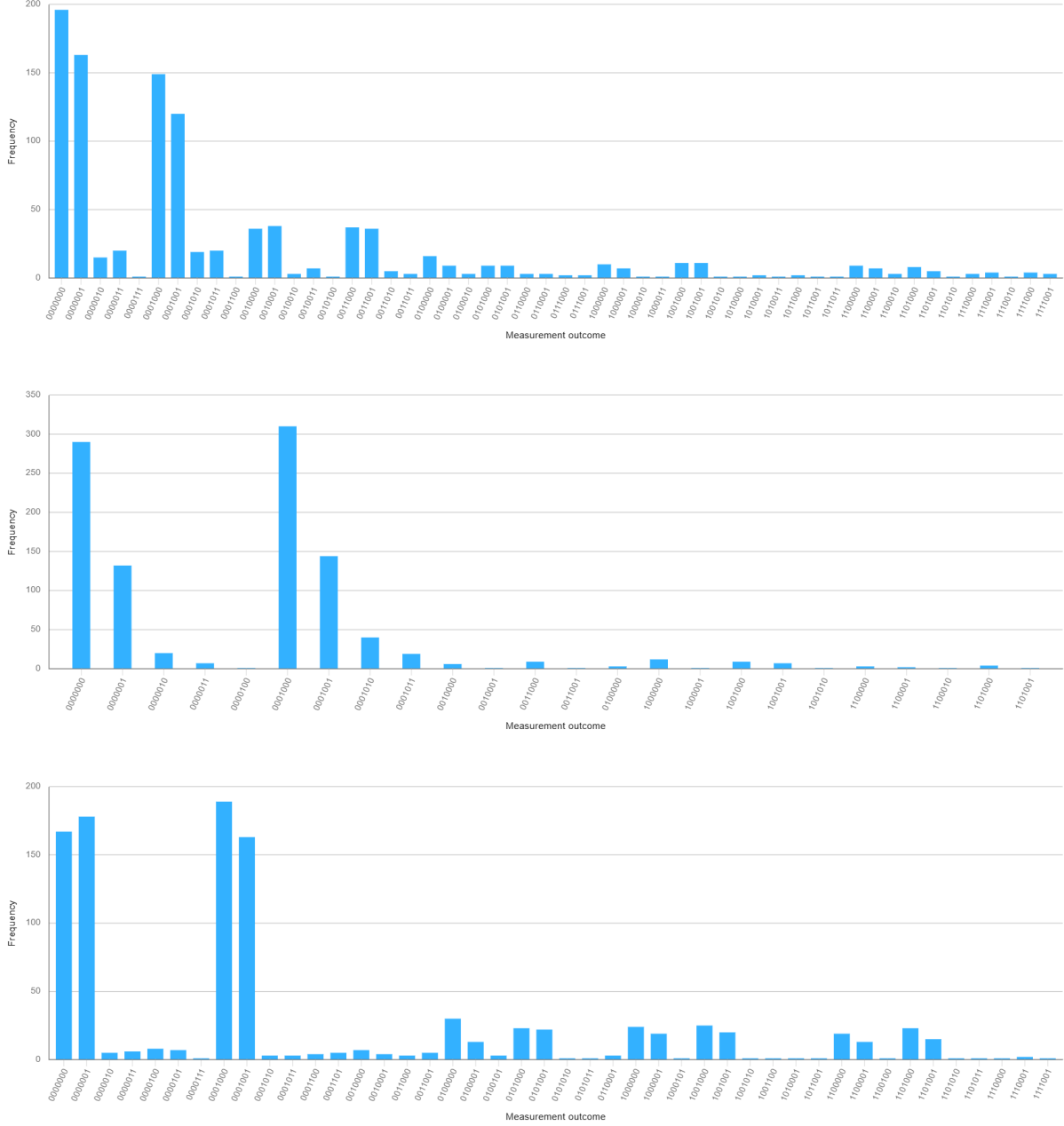


FIG. 5. Measurement outcomes from the second-order digital simulation of the three-level Jaynes–Cummings system executed on the *ibm\_torino*, *ibm\_marrakesh*, and *ibm\_fez* processors. Compared to the first-order implementation, improved confinement within the excitation-conserving subspace and reduced population leakage are observed, particularly on higher-fidelity hardware. Bitstrings are ordered as  $|q_2q_1q_0\rangle$ , where  $q_2$  encodes the truncated cavity photon number.

of how well the Jaynes–Cummings dynamics themselves are preserved. In particular, the degree of confinement within the excitation-conserving subspace and the suppression of symmetry-forbidden transitions directly reflect the fidelity of the simulated light–matter interaction. From this viewpoint, *ibm\_torino* consistently outperforms the other backends, exhibiting the sharpest population localization and the strongest preservation of excitation-number conservation for both first- and second-order implementations. Despite its slightly lower

aggregate fidelity, this backend more faithfully maintains the effective selection rules central to Jaynes–Cummings physics.

Comparing the two digital simulation orders, the second-order Suzuki–Trotter scheme systematically improves state selectivity and reduces unphysical population leakage across all processors, confirming the expected cancellation of leading-order Trotter errors. However, this improvement comes at the cost of increased circuit depth, which amplifies hardware-induced noise and

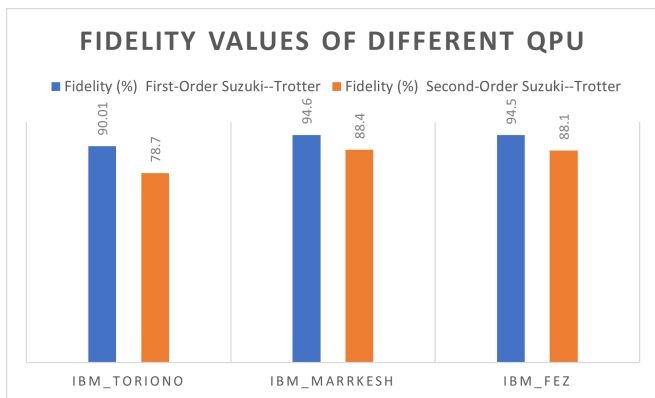


FIG. 6. Fidelity comparison of the three-level Jaynes–Cummings quantum circuit implemented using first-order and second-order Suzuki–Trotter decompositions on different IBM Quantum superconducting processors. The first-order decomposition (blue bars) consistently yields higher circuit fidelity compared to the second-order scheme (orange bars) across all tested devices. Among the considered QPUs, *IBM Marrakesh* and *IBM Fez* exhibit superior performance, while *IBM Torino* shows relatively lower fidelities due to higher accumulated gate and measurement errors.

reduces overall circuit fidelity. As a result, the first-order implementation yields higher aggregate fidelities, while the second-order implementation provides more accurate dynamical behavior, particularly on hardware capable of suppressing correlated errors.

Overall, the results indicate a clear trade-off between algorithmic accuracy and experimental robustness. In an ideal (noise-free) simulator, both first- and second-order Suzuki–Trotter decompositions reproduce the intended unitary evolution exactly, yielding unit (100%) fidelity and confirming that any deviation observed in experiments originates from hardware-induced noise rather than intrinsic Trotterization errors. On real quantum processors, however, second-order Suzuki–Trotter formulas, while algorithmically more accurate for faithful reproduction of three-level Jaynes–Cummings dynamics and excitation-number conservation, require deeper circuits with a larger number of entangling gates and are therefore more susceptible to decoherence and gate infidelities. As a result, the second-order implementation executed on the *ibm.torino* processor emerges as the optimal choice when physical fidelity of the simulated dynamics is prioritized, whereas for shallow circuits and fidelity-limited applications dominated by global error rates, first-order implementations on *ibm.marrakesh* provide superior performance. These observations highlight the necessity of jointly considering ideal baselines, circuit fidelity metrics, and physically motivated observables when benchmarking digital quantum simulations on noisy intermediate-scale quantum devices.

#### IV.2.2. Time-Dependent Population Dynamics

To analyze the dynamical behavior of a three-level atom interacting with a quantized electromagnetic field, we evaluate the time-dependent population probabilities of the atomic energy levels within the Jaynes–Cummings (JC) framework[54]. The populations are obtained from repeated circuit-based simulations performed using IBM Quantum software, where the evolution time is digitally encoded through parametrized rotation angles and the statistics are extracted from projective measurements over multiple shots.

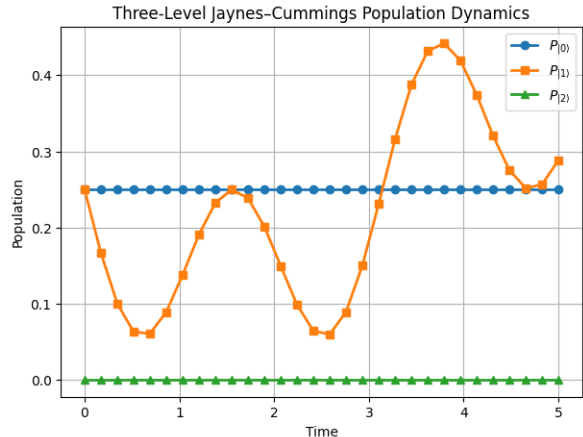


FIG. 7. Time-dependent population dynamics of the three-level atom. The populations of the atomic states  $|0\rangle$ ,  $|1\rangle$ , and  $|2\rangle$  are plotted as a function of the effective interaction time. Pronounced oscillations in  $P_{|1\rangle}$  indicate coherent Rabi dynamics, while the suppression of  $P_{|2\rangle}$  reflects weak access to higher excited states.

Figure 7 shows the temporal evolution of the population probabilities associated with the atomic states  $|0\rangle$ ,  $|1\rangle$ , and  $|2\rangle$ . These populations are defined as

$$P_{|i\rangle}(t) = \langle \psi(t) | (|i\rangle\langle i| \otimes \mathbb{I}) | \psi(t) \rangle, \quad i = 0, 1, 2, \quad (64)$$

where  $|\psi(t)\rangle$  denotes the joint atom–field state at evolution time  $t$ , and the identity operator acts on the truncated cavity subspace.

The underlying dynamics are governed by an effective three-level Jaynes–Cummings Hamiltonian of the form

$$H_{\text{JC}} = \hbar\omega_c a^\dagger a + \sum_{i=0}^2 \hbar\omega_i |i\rangle\langle i| + \hbar g (|1\rangle\langle 0| a + |2\rangle\langle 1| a + \text{h.c.}), \quad (65)$$

where  $\omega_c$  is the cavity frequency,  $\omega_i$  are the atomic transition frequencies, and  $g$  denotes the effective atom–field coupling strength.

In the digital quantum simulation, the continuous time evolution operator  $U(t) = \exp(-iH_{\text{JC}}t/\hbar)$  is approximated by a sequence of single-qubit and controlled rotation gates. The interaction time  $t$  is mapped to the rotation angles of these gates, such that increasing the angle corresponds to longer effective evolution times.

The ground-state population  $P_{|0\rangle}$  remains nearly constant throughout the evolution, indicating stable excitation dynamics without strong redistribution among energy levels. This behavior reflects limited population transfer and confirms that the implemented circuit preserves approximate excitation-number constraints for short interaction times.

In contrast, the population of the first excited state  $P_{|1\rangle}$  exhibits clear oscillatory behavior as a function of time. These oscillations correspond to coherent Rabi oscillations arising from reversible energy exchange between the atom and the cavity field mode. The oscillation frequency and amplitude are determined by the effective coupling strength  $g$  and the degree of coherence maintained during the digital evolution.

The population of the second excited state  $P_{|2\rangle}$  remains negligibly small over the entire evolution window. This suppression indicates that direct population transfer to higher excited states is strongly inhibited by the chosen system parameters and circuit depth. Weak occupation of  $|2\rangle$  may arise through virtual transitions, which introduce small corrections to the effective dynamics of the lower two levels at longer evolution times.

Small deviations from ideal probability normalization can be attributed to cavity-space truncation, finite sampling statistics, and experimental noise in the quantum hardware.

Overall, the observed population dynamics confirm that the system evolution is dominated by the two lowest atomic levels for short interaction times, while higher excited states introduce small but systematic corrections. These results demonstrate the capability of circuit-based quantum simulations to capture time-dependent Jaynes–Cummings dynamics and highlight the importance of higher-level effects in high-fidelity simulations of light–matter interaction models.

## V. CONCLUSION

This work has presented a detailed digital quantum simulation of the three-level Jaynes–Cummings model us-

ing superconducting quantum processors and first- and second-order Suzuki–Trotter decompositions. By systematically encoding the truncated cavity field and multi-level atomic system into qubit registers, we constructed hardware-compatible quantum circuits that faithfully implement the effective atom–field interaction Hamiltonian. The continuous-time dynamics were approximated through carefully calibrated rotation gates, enabling controlled simulation of Rabi oscillations, population transfer, and atom–field entanglement under resonant coupling conditions. The selection rules and excitation-number conservation intrinsic to the Jaynes–Cummings model were enforced through multi-controlled gate structures, ensuring physically meaningful evolution within the encoded subspace.

In addition, the present work differs from related digital quantum simulation studies in both physical focus and methodological emphasis. While previous work primarily addresses general spin–boson models and open-system dynamics using Suzuki–Trotter decompositions, our study targets a physically motivated three-level Jaynes–Cummings light–matter interaction implemented directly on superconducting quantum hardware. We explicitly design first- and second-order digital circuits adapted to a three-level atomic encoding, enforce excitation-selection rules through multi-controlled gate structures, and evaluate performance using both calibration-based circuit fidelity and physically meaningful observables such as excitation-number conservation and population leakage. This combined analysis provides a hardware-aware, model-specific framework for realizing and benchmarking multi-level Jaynes–Cummings dynamics on noisy intermediate-scale quantum devices, going beyond generic digital simulation benchmarks.

- 
- [1] Y. Alexeev, D. Bacon, K. R. Brown, R. Calderbank, L. D. Carr, F. T. Chong, B. DeMarco, D. Englund, E. Farhi, B. Fefferman, et al. Quantum computer systems for scientific discovery. *PRX Quantum*, 2(1):017001, 2021.
  - [2] Sukhpal Singh Gill and Rajkumar Buyya. Transforming research with quantum computing. *JET*, 4:1–8, 2026.
  - [3] Liam Doyle, Fargol Seifollahi, and Chandralekha Singh. Do we have a quantum computer? expert perspectives on current state and future prospects. *Phys. Rev. Phys. Educ. Res.*, 22(1):010101, 2026.
  - [4] Muhammad AbuGhanem. Toward scalable fault-tolerant photonic quantum computers. *J. Supercomput.*, 82(2):51, 2026.
  - [5] Sahar Armaghani and Ali Rostami. Hadamard gate realization based on quantum fourier transform for the creation of quantum numbers in the integrated optical domain. *Sci. Rep.*, 2026.
  - [6] X. Zhang, H.-O. Li, G. Cao, M. Xiao, G.-C. Guo, and G.-P. Guo. Semiconductor quantum computation. *Natl. Sci. Rev.*, 6(1):32–54, 2019.
  - [7] S. M. Frolov, S. R. Plissard, S. Nadj-Perge, L. P. Kouwenhoven, and E. P. A. M. Bakkers. Quantum computing based on semiconductor nanowires. *MRS Bulletin*, 38(10):809–815, 2013.
  - [8] D. Awschalom and D. Loss. *Semiconductor Spintronics and Quantum Computation*. Springer, New York, NY, 2002.
  - [9] J. M. Gambetta, J. M. Chow, and M. Steffen. Building logical qubits in a superconducting quantum computing system. *npj Quantum Inf.*, 3(1):2, 2017.

- [10] S. Kwon, A. Tomonaga, G. L. Bhai, S. J. Devitt, and J.-S. Tsai. Gate-based superconducting quantum computing. *J. Appl. Phys.*, 129(4), 2021.
- [11] Peter Græns Larsen, Anne E. B. Nielsen, André Eckardt, and Francesco Petiziol. Experimental protocol for observing single quantum many-body scars with transmon qubits. *SciPost Phys.*, 20(2):036, 2026.
- [12] Florian Lange, Lukas Heunisch, Holger Fehske, David P. DiVincenzo, and Michael J. Hartmann. Cross-talk in superconducting qubit lattices with tunable couplers—comparing transmon and fluxonium architectures. *Quant. Sci. Technol.*, 11(1):015020, 2026.
- [13] Michael J. Peterer, Samuel J. Bader, Xiaoyue Jin, Fei Yan, Archana Kamal, et al. Coherence and decay of higher energy levels of a superconducting transmon qubit. *Phys. Rev. Lett.*, 114(1):010501, 2015.
- [14] Thomas E. Roth, Ruichao Ma, and Weng C. Chew. An introduction to the transmon qubit for electromagnetic engineers. *arXiv preprint arXiv:2106.11352*, 2021.
- [15] Sergey Bravyi, Oliver Dial, Jay M. Gambetta, Darío Gil, and Zaira Nazario. The future of quantum computing with superconducting qubits. *J. Appl. Phys.*, 132(16), 2022.
- [16] Andreas Bayerstadler, Guillaume Becquin, Julia Binder, et al. Industry quantum computing applications. *EPJ Quantum Technology*, 8(1):25, 2021.
- [17] Benjamin Rempfer and Kevin M. Obenland. Comparison of superconducting nisq architectures. In *Proceedings of the IEEE International Conference on Quantum Computing and Engineering (QCE)*, volume 1, pages 583–592. IEEE, 2024.
- [18] Chuanyu Zhang, Zhide Lu, Liangtian Zhao, Shibo Xu, Weikang Li, Ke Wang, Jiachen Chen, Yaozu Wu, Feitong Jin, Xuhao Zhu, et al. Experimental demonstration of quantum continual learning with superconducting qubits. *npj Quantum Inf.*, 2026.
- [19] Luis Medina-Dozal, Alejandro R. Urzúa, Irán Ramos-Prieto, Ricardo Román-Ancheyta, Francisco Soto-Eguibar, Héctor M. Moya-Cessa, and José Récamier. The physical spectrum of a driven jaynes–cummings model. *Entropy*, 28(1):127, 2026.
- [20] Jorge Casanova, Guillermo Romero, Ion Lizuain, Juan José García-Ripoll, and Enrique Solano. Deep strong coupling regime of the jaynes–cummings model. *Phys. Rev. Lett.*, 105(26):263603, 2010.
- [21] Andrea Smirne, Heinz-Peter Breuer, Jyrki Piilo, and Bassano Vacchini. Initial correlations in open-systems dynamics: The jaynes–cummings model. *Phys. Rev. A*, 82(6):062114, 2010.
- [22] Danilo Cius. Unitary description of the jaynes–cummings model under fractional-time dynamics. *Phys. Rev. E*, 111(2):024110, 2025.
- [23] Caden McCollum and Imran M. Mirza. Exploring photon blockade in multimode jaynes–cummings models with two-photon dissipation. *Phys. Rev. A*, 113(1):013733, 2026.
- [24] Boyan T. Torosov, Stefano Longhi, and Giuseppe Della Valle. Mixed rabi jaynes–cummings model of a three-level atom interacting with two quantized fields. *Opt. Commun.*, 346:110–114, 2015.
- [25] Matteo Bina. *Open Quantum Systems Dynamics within and beyond the Jaynes–Cummings Model*. PhD thesis, Università degli Studi di Milano, 2010.
- [26] Mar Sánchez-Córdova, Jasel Berra-Montiel, and Alberto Molgado. The jaynes–cummings model in phase space quantum mechanics. *Int. J. Theor. Phys.*, 65(2):19, 2026.
- [27] Wen Liang and Zhenhua Yu. Dynamical transition of the generalized jaynes–cummings model: Multiparticle and interparticle interaction effects. *Phys. Rev. A*, 112(3):033710, 2025.
- [28] Shiyao Chong, Xiaolan Liu, Yanzhen Han, Jingjing Du, Jianxiao Liu, Linghui Meng, Yacheng Gao, Changbo Yang, Jian Qi Shen, Junliang Zhang, et al. The long-time behavior of collapse–revival effects in a multiphoton jaynes–cummings model. *J. Phys. Soc. Jpn.*, 94(2):024402, 2025.
- [29] Qi-Cheng Wu, Yu-Liang Fang, Yan-Hui Zhou, Jun-Long Zhao, Yi-Hao Kang, Qi-Ping Su, and Chui-Ping Yang. Efficient and controlled symmetric and asymmetric bell-state transfers in a dissipative jaynes–cummings model. *Chin. Phys. B.*, 35(1):010304, 2026.
- [30] Huanhuan Wei, Jing Tang, and Yuangang Deng. N-photon bundles emission in high-spin jaynes–cummings model. *New J. Phys.*, 26(12):123024, 2024.
- [31] Hai-Ji Li, Li-Bao Fan, Shan Ma, Jie-Qiao Liao, and Chuan-Cun Shu. Exploring photon blockade in a two-photon jaynes–cummings model with atom and cavity drivings. *Phys. Rev. A*, 110(4):043707, 2024.
- [32] Marina Marinkovic and Marina Radulaski. Complexity reduction in resonant open quantum system taviscummings model with quantum circuit mapping. *arXiv*, pages 2208–12029, 2022.
- [33] Yaniv Kurman, Kieran Hymas, Arkady Fedorov, William J Munro, and James Quach. Powering quantum computation with quantum batteries. *Phys. Rev. X*, 16(1):011016, 2026.
- [34] B Sharmila, S Lakshimbala, and V Balakrishnan. Tomographic entanglement indicators in multipartite systems: B. sharmila et al. *Quantum Inf. Process.*, 19(4):127, 2020.
- [35] Daniel Koch, Brett Martin, Saahil Patel, Laura Wessing, and Paul M Alsing. Demonstrating nisq era challenges in algorithm design on ibm’s 20 qubit quantum computer. *AIP Advances*, 10(9), 2020.
- [36] José D Guimarães, Antonio Ruiz-Molero, James Lim, Mikhail I Vasilevskiy, Susana F Huelga, and Martin B Plenio. Optimized noise-assisted simulation of the lindblad equation with time-dependent coefficients on a noisy quantum processor. *Phys. Rev. A*, 109(5):052224, 2024.
- [37] Masuo Suzuki. Quantum statistical monte carlo methods and applications to spin systems. *J. Stat. Phys.*, 43(5):883–909, 1986.
- [38] Johann Ostmeier. Optimised trotter decompositions for classical and quantum computing. *J. Phys. A: Math. Theor.*, 56(28):285303, 2023.
- [39] Benjamin DM Jones, David R White, George O O’Brien, John A Clark, and Earl T Campbell. Optimising trotter-suzuki decompositions for quantum simulation using evolutionary strategies. In *Proceedings of the Genetic and Evolutionary Computation Conference*, pages 1223–1231, 2019.
- [40] Hiroo Azuma. Quantum computation with the jaynes–cummings model. *Prog. Theor. Phys.*, 126(3):369–385, 2011.
- [41] Brian Mischuck and Klaus Mølmer. Qudit quantum computation in the jaynes–cummings model. *Phys. Rev. A*, 87(2):022341, 2013.
- [42] SA Moiseev and SN Andrianov. A quantum computer on the basis of an atomic quantum transistor with built-in quantum memory. *Opt. Spectrosc.*, 121(6):886–896, 2016.
- [43] Adam L Shaw, Anna Soper, Danial Shadmany, Aish-

- warya Kumar, Lukas Palm, Da-Yeon Koh, Vassilios Kaxiras, Lavanya Taneja, Matt Jaffe, David I Schuster, et al. A cavity-array microscope for parallel single-atom interfacing. *Nature*, pages 1–7, 2026.
- [44] Jonas Larson and Themistoklis Mavrogordatos. *The Jaynes–Cummings model and its descendants: modern research directions*. IoP Publishing, 2021.
- [45] Cheng Liu and Jin-Feng Huang. Quantum phase transition of the jaynes-cummings model. *Sci. China-Phys. Mech. Astron.*, 67(1):210311, 2024.
- [46] Celso J Villas-Boas and Daniel Z Rossatto. Multiphoton jaynes-cummings model: Arbitrary rotations in fock space and quantum filters. *Phys. Rev. Lett.*, 122(12):123604, 2019.
- [47] Michael Fleischhauer, Atac Imamoglu, and Jonathan P Marangos. Electromagnetically induced transparency: Optics in coherent media. *Rev. Mod. Phys.*, 77(2):633–673, 2005.
- [48] Ennio Arimondo. V coherent population trapping in laser spectroscopy. In *Prog. Opt.*, volume 35, pages 257–354. Elsevier, 1996.
- [49] Yi-Xiang Liu, Jordan Hines, Zhi Li, Ashok Ajoy, and Paola Cappellaro. High-fidelity trotter formulas for digital quantum simulation. *Phys. Rev. A*, 102(1):010601, 2020.
- [50] Michel Brune, F Schmidt-Kaler, Abdelhamid Maali, J Dreyer, E Hagley, JM Raimond, and S Haroche. Quantum rabi oscillation: a direct test of field quantization in a cavity. *Phys. Rev. Lett.*, 76(11):1800, 1996.
- [51] Andreas Burger, Leong Chuan Kwek, and Dario Poletti. Digital quantum simulation of the spin-boson model under markovian open-system dynamics. *Entropy*, 24(12):1766, 2022.
- [52] Shin Nishio, S Takahiko, and DM Rodney. High fidelity qubit mapping for ibm q. In *Proc. 2nd International Workshop on Quantum Compilation*, 2018.
- [53] Mitali Sisodia, Abhishek Shukla, Alexandre AA de Almeida, Gerhard W Dueck, and Anirban Pathak. A method to improve quantum state fidelity in circuits executed on ibm’s quantum computers. *Can. J. Phys.*, 99(10):924–932, 2021.
- [54] Danilo Cius. Unitary description of the jaynes-cummings model under fractional-time dynamics. *Phys. Rev. E*, 111(2):024110, 2025.